www.MaterialsViews.com

ADVANCED
FUNCTIONAL
MATERIALS
www.afm-journal.de

FULL PAPER

Mapping Morphological and Structural Properties of Lead Halide Perovskites by Scanning Nanofocus XRD

Samuele Lilliu,* Thomas G. Dane, Mejd Alsari, Jonathan Griffin, Alexander T. Barrows, Marcus S. Dahlem, Richard H. Friend, David G. Lidzey, and J. E. Macdonald

Scanning nanofocus X-ray diffraction (nXRD) performed at a synchrotron is used to simultaneously probe the morphology and the structural properties of spin-coated $CH_3NH_3PbI_3$ (MAPI) perovskite films for photovoltaic devices. MAPI films are spin-coated on a Si/SiO_2/poly(3,4-ethylenedioxythiophene): polystyrene sulfonate (PEDOT:PSS) substrate held at different temperatures during the deposition in order to tune the perovskite film coverage. The films are then investigated using nXRD and scanning electron microscopy (SEM). The advantages of nXRD over SEM and other techniques are discussed. A method to visualize, selectively isolate, and structurally characterize single perovskite grains buried within a complex, polycrystalline film is developed. The results of nXRD measurements are correlated with solar cell device measurements, and it is shown that spin-coating the perovskite precursor solution at elevated temperatures leads to improved surface coverage and enhanced solar cell performance.

1. Introduction

Since the seminal work of Kojima et al.[1] in 2009, in which organic–inorganic halide perovskites (OIHPs) were employed

Dr. S. Lilliu, Dr. J. Griffin, Dr. A. T. Barrows,
Prof. D. G. Lidzey
Department of Physics and Astronomy
University of Sheffield
Hicks Building, Hounsfield Road, Sheffield S3 7RH, UK
E-mail: samuele_lilliu@hotmail.it,
s.lilliu@sheffield.ac.uk
Dr. T. G. Dane
European Synchrotron Radiation Facility
BP 220, Grenoble F-38043, France
M. Alsari, Prof. R. H. Friend
Cavendish Laboratory
University of Cambridge
Madingley Road, CB3 0HE Cambridge, UK
Prof. M. S. Dahlem
Masdar Institute of Science and Technology
PO Box 54224, Abu Dhabi, United Arab Emirates
Prof. J. E. Macdonald
School of Physics and Astronomy
Cardiff University
Queens Buildings, The Parade, CF24 3AA Cardiff, UK

for the first time in dye-sensitized solar cells realizing a device with ≈4% power conversion efficiency (PCE), research in the field of perovskite solar cells has grown extensively. In 2012, Lee et al.[2] and Kim et al.[3] reported on mesoscopic perovskite solar cells with ≈10% PCE. This triggered a research "gold-rush," which has attracted considerable resources from both research groups and companies worldwide. Though first devices were based on mesoscopic structures in which the OIHP was included in a nanoporous titanium dioxide structure, it became clear that this structure was not required and that simple planar structures could provide very efficient solar cells.[4] Efforts recently culminated in the fabrication of devices with ≈20% PCE in 2014[4] and ≈21% in late 2015;[5] a performance that suggests OIHP could eventually replace standard crystalline silicon in photovoltaics (PV). The broad range of optoelectronic properties, physical-chemistry aspects, and low-production-cost potential of OIHPs have been widely reported in the literature.[4,6–14] Here, we present an imaging method to simultaneously map the morphological and structural properties of the perovskites with a resolution of 400 nm, and focus on the importance of fine tuning the perovskite film morphology as a route to improve the PCE.

3D OIHPs are described by the formula ABX_3, where A is a bulky monovalent cation (e.g., $CH_3NH_3^+$), B is a divalent metal halide cation (e.g., Pb^{2+}, Sn^{2+}, Ge^{2+}), and X is a monovalent halogen anion (e.g., I^-, Br^-, Cl^-). Structurally, the A cation is surrounded by a BX_6 octahedron, in which A is bonded to 12 X anions.[15,16] To date, the most widely studied perovskite for PV applications has been methylammonium lead triiodide ($CH_3NH_3PbI_3$, which has been informally named MAPI). Several methods have been explored to fabricate perovskite layers, with solution deposition techniques under "ambient" conditions being the most industrially attractive in terms of large area coating and low production cost.[8,17–20] The simplest deposition method is the so-called "one-step" process,[18,21] in which a precursor ink is prepared by dissolving a mix of an ammonium salt (e.g., CH_3NH_3I, also known as methylammonium iodide (MAI)) and a lead salt (e.g., PbI_2, $PbCl_2$, or $PbAc_2$) in a solvent such as N,N-dimethylformamide (DMF). This ink can then be deposited using a variety of methods including spin-coating,[17] inkjet-printing,[19] and spray-coating.[18] The

as-coated "precursor" film is then thermally annealed to enable its conversion into the MAPI perovskite.[22] The perovskite layer is polycrystalline,[23,24] with single crystallites having a typical lateral size ranging from a few tens of nanometers to 10–100s of microns, as evidenced by scanning electron microscope (SEM) imaging.[24–26] Perovskite grains are usually separated by voids or grain boundaries.[27] There has been some debate on the effect of grain boundaries,[28–30] with recent reports pointing toward the beneficial effect of their minimization[23,24,31,32] as this reduces the defect density and thus charge traps, which leads to improved charge extraction and thus more efficient solar cells.[26] Achieving a uniform film coverage in which the polycrystals cover the entire solar cell active area without gaps or pin-holes[26] is another key morphological requirement to obtain efficient devices. Thus an ideal perovskite layer in a solar cell should consist of a smooth and flat single crystal without voids or grain boundaries. While this ideal morphology is hard to obtain by solution casting, larger grains and smoother films with fewer grain boundaries can be obtained by employing processing additives[33,34] to the precursor solution,[34,35] by using different solvent[35] and lead salts,[25] and by using solvent annealing.[23,31]

To date, the most widely employed techniques to investigate the crystal structure and morphology of perovskite films have been SEM and X-ray diffraction (XRD). SEM has mainly been employed to image surface structure at both low and high magnifications. When combined with focused ion beam, it is also able to image cross-sections through complete solar cells, although this technique creates local damage. Perovskite crystallites can often be distinguished in as-spun precursor films; however, upon annealing for times longer than 20–30 min, these crystallites tend to merge in the final perovskite film.[6,36] This makes the isolation of single crystallites and the determination of the statistics of lateral grain size and shape difficult.[36] A further limitation is that both SEM and other scanning probe microscopy techniques are surface-sensitive, with the bulk of the material being largely inaccessible using conventional imaging methods.

The internal atomic scale structure of an OIHP is typically determined by X-ray diffraction techniques. Among the various possible geometries, the sample can be either close to parallel (grazing incidence) or perpendicular (transmission geometry) to the X-ray beam. The main advantages of a grazing geometry over a transmission geometry are that (i) the preferential orientation of the crystallites with respect to the sample surface can be probed, and (ii) different penetration depths can be probed by varying the incident angle. The X-ray scattering technique can be further classified by the distance between the sample and the detector. In wide-angle X-ray scattering, the sample-detector distance is relatively short (e.g., 0.3 m) and the measured diffraction rings or spots can be used to determine the crystallographic structure of the film (such as domain sizes that are typically below 100 nm, lattice constants, etc.). In small angle X-ray scattering, the sample-detector distance is relatively large (e.g., 10 m) and the crystal size distribution that is probed is much larger (typically between 10 and 400 nm). In grazing incidence wide angle X-ray scattering (GI-WAXS), grazing geometry is combined with short sample-detector distance.[37] GI-WAXS has proved to be a powerful technique for in situ studies of one-step deposited perovskite films, where the effect of thermal annealing can be determined in real time.[27,36,38] Another valuable technique consists in combining grazing incidence geometry with large sample-detector distance, and is referred to as grazing incidence small angle X-ray scattering (GI-SAXS).[37] GI-SAXS has been used to investigate the size distribution of crystals within "two-step" deposited perovskite films at different penetration depths[39] and the distribution of crystals within perovskite films deposited using a "one-step" method,[40] with both studies identifying crystals having characteristic dimensions of up to 400 nm. We note that larger size crystals can be probed by employing larger sample-detector distances (e.g., 30 m) using a technique called ultrasmall angle X-ray scattering.

In this work, we are interested in perovskite crystals having very large length scales (up to ≈20 μm) and in combining existing X-ray techniques with scanning probe techniques to create combined morphological and spatial maps of a perovskite film. Conventional X-ray beams used in GI-WAXS and GI-SAXS have a cross-sectional area of 0.1–1 mm^2, and are thus orders of magnitude larger than the critical dimensions of most morphological features in OIHP films. For this reason, the observed diffraction patterns represent an ensemble average of structural features determined over a macroscopic area. Information on the crystallographic structure (in the case of GI-WAXS) and particle size distribution (GI-SAXS) is then determined by fitting a model to the observed data. Such an approach offers great insight to the structural properties of materials with well-defined structures, however the reliance on models means that local inhomogeneity cannot be well described.

Fortunately, recent developments in X-ray focusing optics at high brilliance third generation synchrotron light sources now permit the routine generation of intense, micron and submicron diameter X-ray beams under ambient conditions.[41,42] By raster scanning an X-ray "nanobeam" across a sample, it is possible to combine real-space imaging with atomic scale structural information afforded by XRD. Such scanning nanofocus XRD (nXRD) techniques have been employed to resolve local variations in structure across a broad range of materials and research fields including polymer and biopolymer fibers,[43] organic electronic materials,[44–46] macromolecular crystallography,[47] biological tissues,[48,49] semiconductor nanostructures,[50,51] and superconductors.[52–54] However, despite the wealth of structural information offered by nXRD, this technique has yet to be employed to examine the structure of OIHP films. We note that combining nXRD with grazing incidence geometry to probe local differences between surface and bulk along with the orientation of individual crystallites would be highly attractive. However, this is practically unfeasible due to the elongated footprint of the beam impinging on the sample surface; below the critical angle, the beam footprint on the sample is still highly focused in a direction normal to the beam, but has a length that is hundreds of microns along the beam direction. Therefore, the only feasible option is to combine nXRD with a transmission geometry. The main drawback in working in transmission geometry is that potential differences between surface and bulk are averaged, as the beam probes the entire depth of the film.[39] Nevertheless, we demonstrate that nXRD in transmission geometry can be used to gather spatially resolved morphological and structural information on films of the archetypal

$CH_3NH_3PbI_3$ perovskite in thin films that can be used directly in planar solar cell architectures. This method provides a way to determine information that could not be accessed using conventional GI-WAXS or GI-SAXS. Using nXRD, we provide detailed information about the lateral structure of the film with a lateral resolution of 400 nm, although this technique cannot determine film structure normal to the plane of the film. In our work, we develop a method to select and visualize grains diffracting according to a specific Miller plane using custom-made analysis software. Using this method, we show that nXRD is able to resolve the extent of individual perovskite grains buried within a polycrystalline film (grain segmentation). We then use nXRD and SEM to demonstrate that the perovskite film coverage across the substrate can be controlled by varying the temperature of the substrate during spin-coating. We conclude by showing that solar cells with a perovskite layer cast on a substrate held at a relatively high temperature result in devices with higher PCE.

2. Results and Discussion

We prepared three types of $CH_3NH_3PbI_3$ (MAPI) perovskite films by spin-coating a precursor solution made of methyl-ammonium iodide mixed with lead chloride with a 3:1 molar ratio in DMF, on ≈725 μm thick Si/SiO_2 substrates coated with a ≈40 nm thick interlayer of poly(3,4-ethylenedioxythiophene) polystyrene sulfonate (PEDOT:PSS): (1) cold-spun samples (here termed "cold," spun on a substrate held at room temperature); (2) medium-spun samples ("medium," spun with the substrate at an initial temperature of ≈75 °C); (3) hot-spun samples ("hot," spun with the substrate at an initial temperature of ≈90 °C). The film thicknesses after annealing for the cold, medium, and hot samples measured with a profilometer were ≈350, ≈500, and ≈650 nm, respectively.

Typical SEM images of annealed cold, medium, and hot MAPI films are shown in **Figure 1**. It can be seen that improved film coverage is obtained at increased substrate temperatures during spin-coating. This result confirms previous reports that have shown that casting the precursor onto a relatively warm substrate can assist the formation of a more uniform morphology.[18,55] Here, the creation of a uniform precursor film is important for producing a uniform perovskite film; a result likely explained by the reduction in film volume caused by

thermal annealing.[36] As seen in Figure 1, the perovskite grains appear to have merged together,[36] making it difficult to define the location of the grain boundaries; an effect that limits grain segmentation analysis. It is also clear that the films are multi-layered, although it is not possible to resolve such subsurface structure using SEM. Note, we have used GI-WAXS to study these cold, medium, and hot samples (see the Supporting Information), however this measurement does not indicate significant morphological differences between the three samples.

2.1. Scanning nXRD

Scanning nXRD measurements were performed at the ID13 beamline (ESRF, Grenoble, France), where each sample was placed on a holder mounted on high-speed xyz piezo scanning stages. An optical microscope with a 50× magnification was first used to align the sample into the focal plane of the X-ray beam and to image a specific region of interest defining the center of the nXRD scan (**Figure 2**a). Figure 2c,f,i shows the optical micrographs corresponding to the region in which nXRD measurements were performed. The microscope was then retracted (Figure 2b) and the sample was illuminated in transmission mode with a monochromatic beam (energy ≈ 14.85 keV) focused into a $200 × 200$ nm² spot size, which was measured at the full width at half maximum (FWHM) of the horizontal and vertical beam profile. Section 3.1 in the Supporting Information gives further details of the beam characterization measurements. The sample was then raster scanned with respect to the beam over a $40 × 40$ μm² area. A scan step-size of ≈400 nm along the horizontal and vertical direction was chosen to minimize strong scattering from the beam tails.

Diffraction patterns were collected at each point of the raster scan using a 2D detector. A full scan consisted of 10 201 diffraction images. Note that as the sample was not rotated during measurement, nXRD will not generally detect peak scattering intensity due to the angular separation between the scattering vector and the reciprocal lattice vector for a specific crystalline grain. To analyze the data, we developed a MATLAB application, details of which are included in the Supporting Information. Montages of the diffraction images were constructed by placing each full diffraction image at the spatial coordinate at which it was collected (see inset Figure 2b). The sparse patterns of these montages are shown in Figure 2d,g,j for the three samples.

Note that after background subtraction (see Section 3.2 "Noise Removal and Average Diffraction Pattern" in the Supporting Information), the majority of pixels in each diffraction pattern had an intensity value of zero, meaning the data could be stored as sparse matrices. The development of software that could handle sparse matrices was essential for this step. In fact, a montage of $101 × 101$ images (each of 17 MB in the standard synchrotron *.EDF format), would have resulted in a ≈170 GB image, which could not have been easily visualized. Instead, by displaying the montage as a sparse pattern we can explore multiple diffraction patterns in real
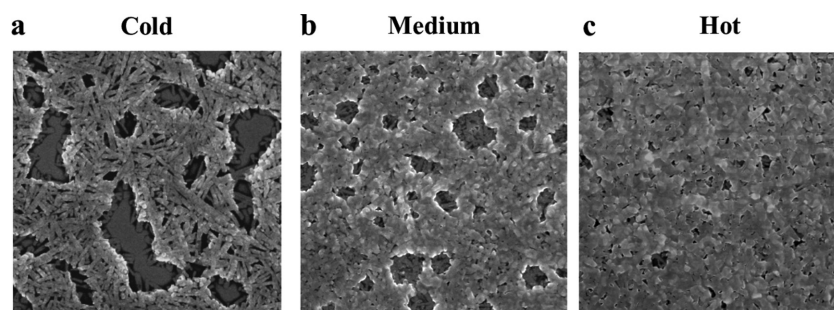

Figure 1. SEM scans of a) cold, b) medium, and c) hot spun MAPI films. In each case, the scan area is $40 × 40$ μm². It can be seen that the film surface coverage increases as the deposition temperature is increased.
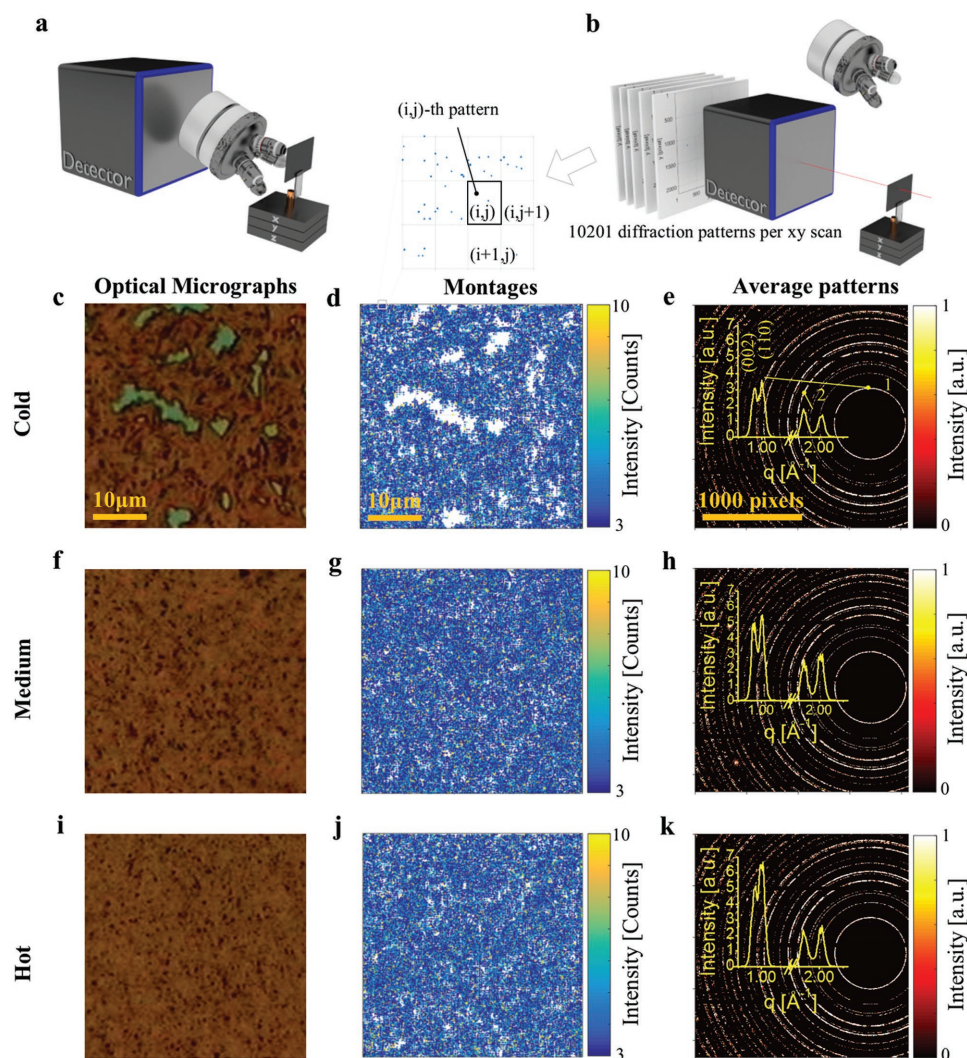
Figure 2. Summary of measurements performed with scanning nanofocus XRD (nXRD). a) nXRD scan area selection with the optical microscope. b) Setup during nXRD measurements. The inset in (b) illustrates the construction of a montage, where "(i,j)-pattern" indicates single diffraction patterns from the 10 201 diffraction pattern dataset in a raster scan, where i is the row scan index and j is the column scan index. c,f,i) 40×40 μm^2 optical micrographs acquired before the scan on the scan area for the cold, medium, and hot samples. d,g,j) 40×40 μm^2 nXRD montages for the cold, medium, and hot sample. e,h,k) 2167×2070 pixel average diffraction patterns recorded from the cold, medium, and hot sample. The insets display portions of the azimuthally integrated line profiles around the two (indicated as "1" and "2") main double perovskite reflections around $q \approx 1$ Å^{-1} ((002) and (110) peaks) and $q \approx 2$ Å^{-1} ((004) and (220) peaks). Note that the x-axis is broken between 1.03 and 1.97 Å^{-1}.

time from a chosen region of interest and vastly reduced the processing time required for further data analysis. The construction of a montage allows us to immediately establish a correlation between the structural texture of the film and its morphological properties (approximating the local intensity of X-ray scattering as is evident in Figure 2). This is particularly evident for the cold sample. Here, the optical micrograph (Figure 2c) shows clear discontinuities in the film, with the green regions corresponding to the underlying Si/SiO$_2$ substrate. The same regions can be seen in the corresponding montage (Figure 2d) and correspond to zones in which no diffraction peaks were observed (plotted using white color on the montage image). The surface coverage, quantified as the ratio between the images that contain diffraction peaks and the total number of images in a scan (10 201), is ≈92% for the cold

sample. In contrast, the medium and hot samples are characterized by a much higher degree of surface coverage (≈99%). Interestingly, in these films, the montages reveal details that are not evident from the optical micrographs. In fact, from the optical micrographs, one would conclude that there is an almost perfect coverage in the medium and hot samples; however, the montages show small voids, corresponding to regions in which no diffraction peaks were observed.

We can also construct an average diffraction pattern as $I_{av} = \left(\sum_{i=1}^{N} I_n \right) / N$, where I_n is the matrix corresponding the n-th image in a scan and N is the total number of images in the raster scan (see Figure 2e,h,k for the three samples). This average diffraction pattern would be equivalent to one collected in a single acquisition with a beam having a footprint 200 times
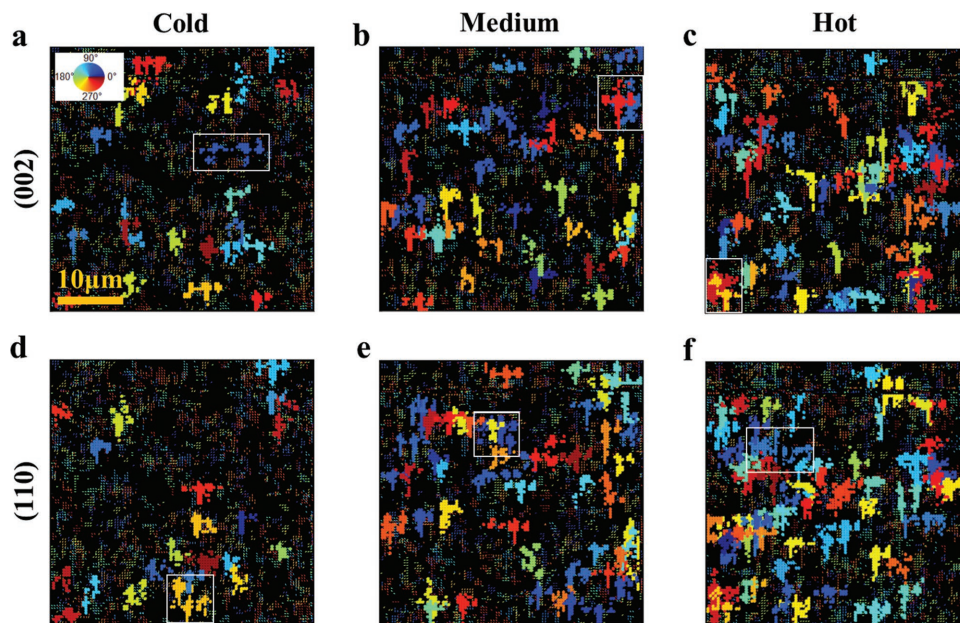
www.MaterialsViews.com

ADVANCED
FUNCTIONAL
MATERIALS
www.afm-journal.de

FULL PAPER

Figure 3. a–f) $40 \times 40\ \mu m^2$ quiver plots highlighting (002) and (110) perovskite grains larger than 4 μm^2. In a quiver plot, the value of one or more (002) or (110) diffraction spot peak angle (χ_p) is represented using an arrow with its center located in the spatial position where the diffraction spot was acquired, and with an orientation and color corresponding to χ_p. As the plots are resized for visualization purposes, the arrows appear as single pixels. Clusters of pixels having the same color represent single grains having the same orientation χ_p. The white boxes indicate the largest grains. Grains with different χ orientations are colored in a different way according to the colormap shown in inset in (a).

larger, i.e., $40 \times 40\ \mu m^2$. It can be seen in Figure 2e,h,k that the average scattering patterns for the cold, medium, and hot samples are very similar. To analyze this in more detail, we extract azimuthally integrated line profiles from the average patterns, which are partially plotted in the insets in **Figure 3**e,h,k showing the (002), (110), (004), and (220) reflections. As in other reports,[56,57] we can distinguish between the (002) and (110) peaks which are usually classified as the first main perovskite peak. Indeed, in other reports, this double peak is often simply identified as the (110) peak.[6,25,58–60] This is likely due to poor instrumental resolution that does not allow these two reflections to be resolved. One should note that such a double peak converges into a single peak (100) at temperatures greater than 54–57 °C, when the perovskite phase converts from tetragonal (β-phase) to cubic (α-phase).[56,61] Clearly, approximating such a double peak as a single peak inevitably leads to inaccuracies in the calculation of crucial parameters such as the lattice constants. Since both MAI:PbCl$_2$ and MAI:PbI$_2$ precursor solutions crystallize as CH$_3$NH$_3$PbI$_3$ (MAPI),[25] the line profiles (from $q = 0.9$ to 4.6 Å^{-1}) were used to refine the MAPI tetragonal structure from ref. [62]. On the basis of our measurements, we determine $a = b = 8.887 \pm 0.001$ Å and $c = 12.663 \pm 0.005$ Å as the average lattice parameters for the three samples, which is in good agreement with the refined β-phase[61] MAPI crystals reported by Liang et al. ($a = b \approx 8.874$ Å and $c \approx 12.670$ Å),[57] Im et al. ($a = b \approx 8.883$ Å and $c \approx 12.677$ Å),[63] Kojima et al. ($a = b \approx 8.855$ Å and $c \approx 12.659$ Å).[1] Other authors have reported a shorter c lattice constant for perovskites obtained from the PbCl$_2$ lead salt ($c \approx 11.24$ Å),[2,6,64] which was explained as resulting from the incorporation of Cl in the lattice structure.[64] Others reported a minor difference between perovskites

obtained from PbI$_2$ and PbCl$_2$ lead salts ($c \approx 12.67$ Å for PbI$_2$ and $c \approx 12.64$ Å for PbCl$_2$), which was attributed to a degree of Cl-doping in the film.[65] Discrepancies between these and our measurements could be due to different instrumentation and processing methods (e.g., annealing temperature and time), different MAI batches, or sample treatment. From our measurements, we determine that perovskites deposited from PbI$_2$ and PbCl$_2$ lead salts have the same MAPI crystal structure.[25] Due to the similarities between the average structural data of the three samples, we therefore conclude that the different processing temperatures explored here do not affect the unit-cell crystal structure of the perovskite films.

We now focus on the texture of the three samples and illustrate a method for performing grain segmentation and quantitative analysis. Here, we focused on the (002) and (110) reflections, although the method can be extended to higher order reflections. To do this, a circular region of interest was defined that included only these reflections (note that in the following discussion, the terms "image" and "diffraction image" refer to the circular region of interest). Diffraction spots in each image were identified and assigned to (002) or (110), and then analyzed. For each spot, peak values of q_p, χ_p, and intensity I_p were extracted, where q (Å^{-1}) and χ (degrees) indicate the scattering vector in polar coordinates and the subscript p stands for "peak." Note that the angle χ should not be confused with a diffractometer circle. The spatial coordinates of the n-th scan and χ_p of the k-th diffraction spot were then used to perform grain clustering in an attempt to identify distinct grains having a specific χ orientation. The assumption made in the clustering procedure is that diffraction spots that are adjacent both in spatial coordinates and in reciprocal space coordinates originate from the same grain.

FULL PAPER

Once single grains were clustered, spatial maps of q_p, χ_p, intensity, FWHM, etc., were constructed, allowing us to determine the grain size with an accuracy of ±200 nm based on the spatial location of the diffraction spots. The grain size reported here corresponds to the lateral area (parallel to the substrate and perpendicular to the X-ray beam) of the perovskite platelets. From the clustered diffraction-spot maps, we also constructed quiver-plots. In a quiver plot, the value of χ_p determined is represented using an arrow with its center located in the spatial position from which the diffraction spot was acquired, and with an orientation and color corresponding to χ_p. Such quiver plots allow multiple arrows to be visualized, even if they are centered at the same spatial location; a situation that occurs due to the overlap of grains having different values of χ_p. Using the clustering and visualization tools developed here, we are able to selectively classify grains having a specific size or other properties. In Figure 3, we show quiver plots generated for the (002) and the (110) reflections for the cold, medium, and hot films, where the thicker arrows, which at the present zoom appear as dots (magnifications are available in the Supporting Information). Although all data are plotted in this figure, quiver arrows are highlighted for grains having a size larger than 4 μm^2 using a color scale that indicates the relative orientation of the grain χ_p. We also highlight the largest grain imaged in each sample using a white rectangular box. It can be seen that the number of grains having a lateral size larger than 4 μm^2 correlates with increasing spin-coating temperature. The grain size statistics reported in Table 1 confirm that the maximum grain size increases as the spin-coating temperature increases.

Before discussing our results in detail, we briefly consider the spatial resolution of our measurements. As shown in Section 3.1 (Supporting Information), the FWHM of the X-ray beam at the sample surface is ≈200 nm, however the step size used to construct the image (400 nm) is larger than this and thus defines the spatial resolution of the measurement (i.e., we are not able to distinguish among grains smaller than 400 nm). While the beam size as defined by the FWHM is roughly the same in the horizontal and vertical directions, we find that there is a slightly larger beam tail at one side of the vertical beam profile (see Section 3.1, Supporting Information), which generates additional diffraction spots from adjacent scan points along the vertical direction. This effect results in a systematic distortion ("bleeding") in many grains along the vertical direction (vide infra).

We plot spatial maps of the peak intensity for the largest (002) and (110) grains (highlighted by using the white boxes in

Figure 3) for the cold, medium, and hot samples in **Figure 4**. These maps present the highest values at the center of the grain, thus indicating that crystallites are thickest in the center of the grains. Analogous maps for the lattice constants, FWHM, etc., can also be generated, as shown in the Supporting Information.

Figure 5 plots histograms of lateral grain size determined from the (002) and (110) reflections. The ability to extract the distribution of grain sizes (which follows a power law) provides more information than the usually quoted "average grain size" determined from the measured peak width. It also gives a grain size distribution that is not affected by microstrain, lattice distortions, inhomogeneity, and instrumental broadening contributions that can affect peak width analysis. From Figure 3, it can also be seen that the largest grains in each quiver plot often overlap with other grains. The histograms of the number of diffraction spots per diffraction pattern (i.e., circular region of interest) in **Figure 6**, show that the degree of overlap is low in the cold cast sample, and higher in the medium and hot sample. This trend, in fact, correlates well with film thickness; i.e., the thicker samples are characterized by more overlapping crystallites. Although we are unable to determine the thickness of these grains, the ability to visualize overlapping (or buried) grains and grains with specific properties, such as size or orientation, makes this technique extremely powerful.

2.2. The Role of Substrate Temperature on Solar Cell Efficiency

Finally, we investigated the effect of substrate deposition temperature on the photovoltaic performance of a perovskite solar cell. Solar cells were fabricated and measured as described in the Experimental Section. The device architecture used was glass/indium-tin-oxide (ITO, 100 nm)/PEDOT:PSS (30 nm)/perovskite/[6,6]-phenyl-C71-butyric acid methyl ester ($PC_{70}BM$) (120 nm)/Ca (5 nm)/Al (100 nm). Solar cells were measured under standard light conditions (100 mW cm^{-2}, AM1.5G illumination), without initial light soaking and without pre-biasing. In **Figure 7**, we plot current-density versus voltage curves recorded from the devices that were deposited from a precursor solution on to cold, medium, or hot substrates. To ensure statistical significance, we measured between 11 and 16 pixels for each deposition condition. **Table 2** displays average and champion device metrics for the different conditions, recorded using forward (−1 to +1) and reverse (+1 to −1) JV scans. It can be clearly seen that the solar cell performance is maximized when devices are deposited onto a hot substrate (a champion (average ± std) PCE of 12.8% (11.9 ± 0.8)% is obtained from the reverse scan). We find that the improvement in device efficiency mainly occurs as a result of improved J_{sc}, which is consistent with improved film coverage and enhanced optical absorption occurring in precursor films deposited onto a hot substrate.

3. Conclusions

We have employed synchrotron scanning nXRD to probe the morphology and the structural properties of spin-coated

Table 1. Statistics for the (002) and (110) lateral grain sizes for the cold, medium, and hot samples calculated using the data plotted in Figure 5.

		Maximum grain size [μm^2]	Number of grains larger than 4 μm^2
(002)	Cold	9.6	24
	Medium	14.4	39
	Hot	16.48	52
(110)	Cold	12.96	21
	Medium	12.8	49
	Hot	18.88	60

www.MaterialsViews.com

ADVANCED
FUNCTIONAL
MATERIALS
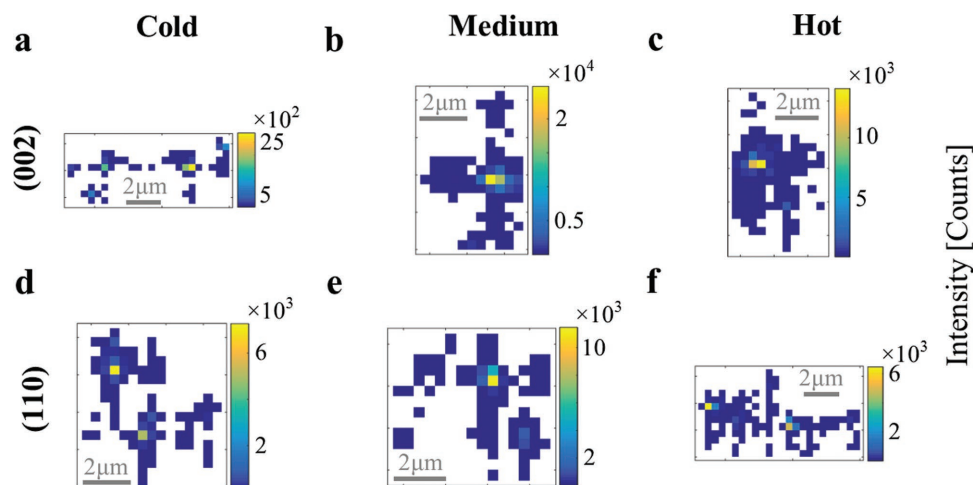www.afm-journal.de

FULL PAPER

Figure 4. a–f) Spatial maps of the peak intensity for the largest (002) and (110) grains highlighted by the white boxes in Figure 3. Scale bars are shown inside the maps and the color bars indicate the intensity. These maps show the highest intensities around the center of the crystallite, which correspond to increased thickness.
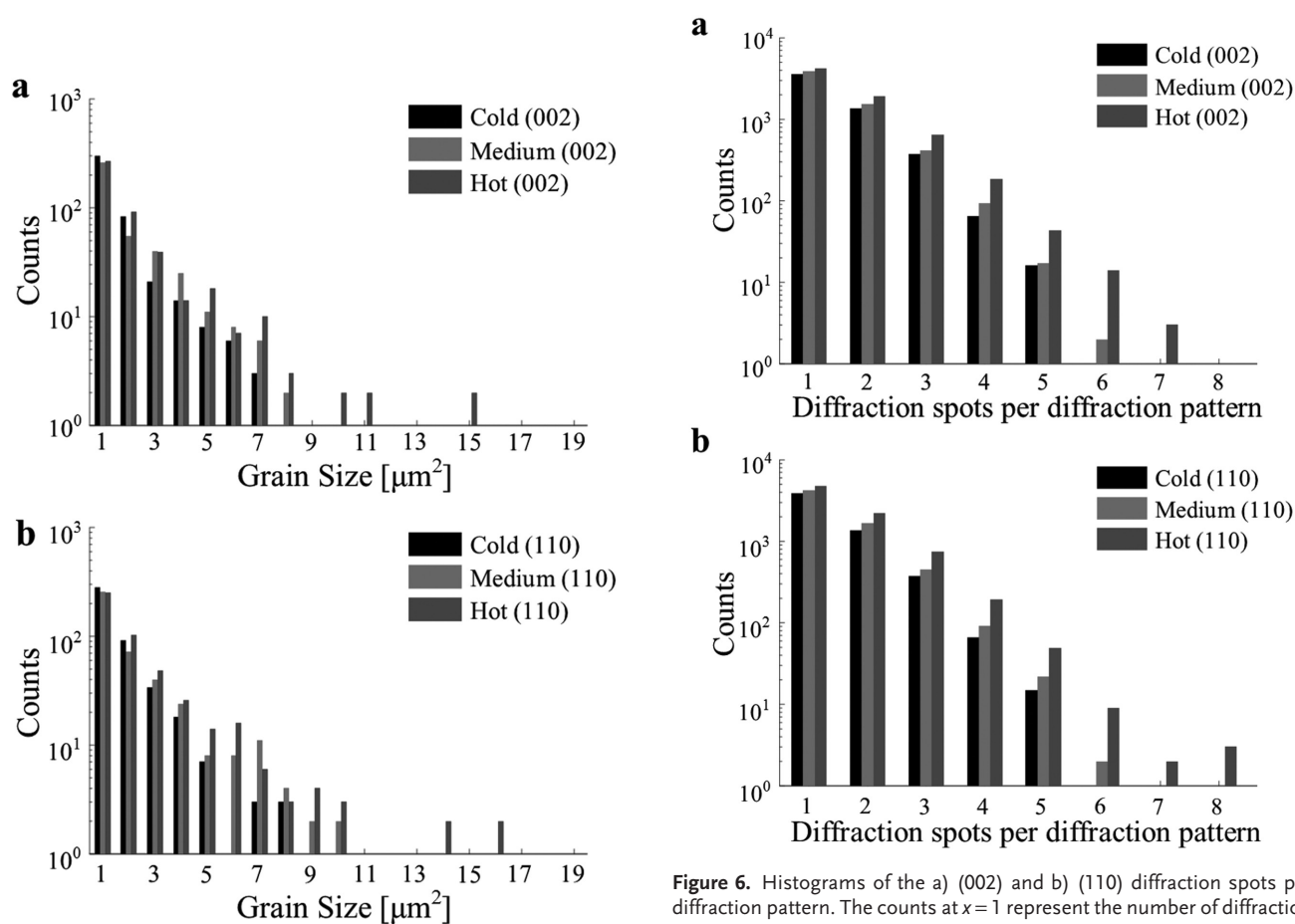

Figure 5. Histograms of the a) (002) and b) (110) lateral grain sizes for the cold, medium, and hot-spun samples. The grain size is shown as an area in μm^2. Values were extracted using the clustering method based on the quiver plot. The histogram bin is 1 μm^2 wide. Counts are expressed on a logarithmic scale.
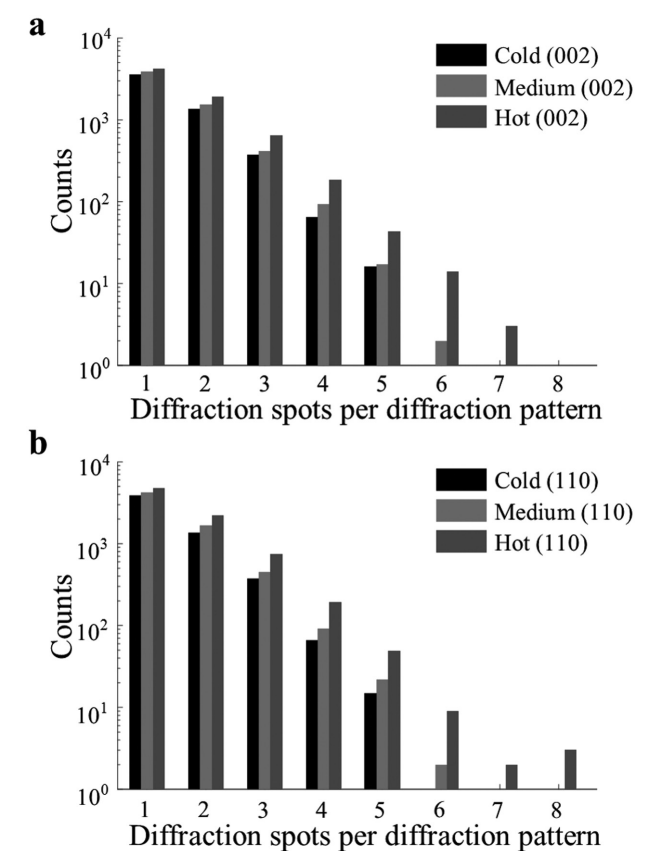

Figure 6. Histograms of the a) (002) and b) (110) diffraction spots per diffraction pattern. The counts at $x = 1$ represent the number of diffraction images with just one (002) or (110) diffraction spot (containing at least 40 pixels). The counts at $x = 2$ represent the number of diffraction images with two (002) or (110) diffraction spot (containing at least 40 pixels), and so on. These histograms show that the hot cast samples systematically display the largest number of overlapping grains. Counts are expressed on a logarithmic scale.
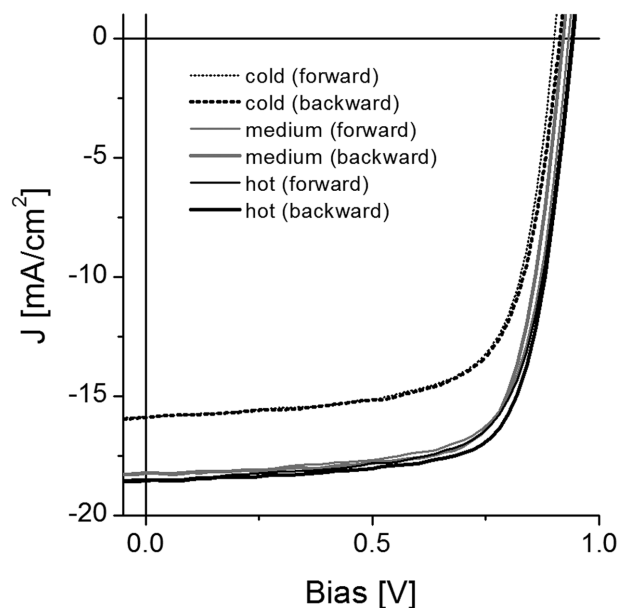
Figure 7. Current-density versus voltage measurements for the best cold, medium, and hot spun perovskite solar cells. The measurements were recorded without any light soaking, both from forward (from −1 to 1 V) and reverse (from 1 to −1 V) voltage sweeps.

$CH_3NH_3PbI_3$ (MAPI) films used in solar cell applications. In particular, using nXRD, we are able to unambiguously perform grain segmentation and extract the lateral size, strain, and orientation of individual perovskite platelets. In contrast to SEM, nXRD performed in transmission geometry provides a picture of overlapping grains located at different depth within the film, although no information on the relative depth of individual grains can be extracted. Our technique allows us to determine morphologically relevant information (such as surface coverage and grain statistics) from perovskite films that were spin-cast on substrates held at different temperatures, with the size-distribution of crystal grains following a power law. We confirm that films coated on substrates held at relatively high temperature have a lower density of pinholes and are characterized by larger grain size. We find that such films can be used to create solar cell devices having improved light harvesting abilities and thus enhanced power conversion efficiency.

4. Experimental Section

Some of the details regarding sample and solar cell preparation had already been reported in the previous works[18,36,40] and were reproduced here for clarity.

SEM and nXRD Samples Preparation: Si/SiO$_2$ substrates (wafer thickness ≈725 μm, oxide thickness ≈300 nm) were cleaned by sonication in isopropyl alcohol and deionized water (10 min each), and dried with compressed nitrogen before use. MAI powder (>98% purity) was synthetized as per the previous work.[18] MAI and PbCl$_2$ (98% purity) were dissolved in sequence (3:1 molar ratio) into *N,N*-dimethylformamide (664 mg mL^{-1}), heated at ≈75 °C overnight to facilitate dissolution of solid material, cooled to room temperature, and then filtered through a 0.45 μm PTFE filter before use. Samples were prepared in ambient conditions (lab temperature ≈24 °C, relative humidity ≈30%). A ≈40 nm layer of PEDOT:PSS (Heraeus Clevios P VP AI 4083) was spin-coated (5000 rpm, 30 s) on the Si/SiO$_2$ substrate immediately before the deposition of the perovskite layer. The three sets of samples ("cold," "medium," and "hot") were prepared under ambient conditions (lab temperature of ≈24 °C at a relative humidity of ≈30%). In all cases, the temperature of the precursor ink was held at 75 °C before it was spin-cast, with all coating performed. The perovskite films were all spin-coated at 4000 rpm for 30 s. The "cold spun" samples were spin-coated on a substrate held at room temperature. The "medium spun" samples were prepared by spin-coating a substrate transferred from a hotplate at ≈90 °C. The time required to transfer the substrate from the hotplate to the spin-coater chuck was 5 s. Using a thermometer with a k-type wire thermocouple, it was estimated that the substrate at the beginning of the spin-coating was at ≈75 °C (the temperature drop during the spin-coating process as there was no means of controlling it). The "hot spun" sample was prepared as the "medium spun" sample, but with the hotplate set at ≈120 °C. In this case, the substrate at the beginning of the spin-coating was at ≈90 °C. The samples were then annealed under ambient conditions for 90 min on a hotplate set to a temperature of 90 °C, and stored under nitrogen before the measurement.

SEM: SEM images were taken with an FEI Nova NanoSEM, employing an incident beam voltage of 20–30 kV together with a secondary electron detector.

nXRD Beamline Setup: A monochromatic beam of λ = 0.8349 Å was focused by crossed linear refractive silicon nanofocusing lenses[66] to a spot size of ≈200 × 200 nm^2, with an incoming flux of ≈5 × 10^{10} photons s^{-1}. Additional lead shielding and an electron microscopy aperture (20 μm diameter) were used to remove any parasitic background scattering. All measurements were performed under ambient conditions (lab temperature ≈24 °C, relative humidity ≈40%).

Samples were mounted on a high speed *xyz* piezo scanning stages on top of a coarse positioning 6-axis hexapod (Physik Instrumente) such that the perovskite material faced downstream to the incoming X-ray beam. Samples were positioned and aligned to the focal plane of the X-ray beam using an on-axis microscope. This microscope was also used to select regions of interest for measurement and to record optical micrographs. Data were recorded on an EIGER 4M detector (Dectris) with 2168 rows × 2070 columns and pixel size of 75 × 75 μm^2, using an exposure time of 0.1 s. The detector was placed at a distance of 0.194 m from the sample. The detector position and geometry were calibrated by recording a diffraction pattern of the standard calibration material corundum (α-Al$_2$O$_3$) and using the pyFAI-calib calibration routine, which yielded the distance, point-of-normal-incidence and detector rotation angles.[67]

Fabrication of Solar Cells: Glass substrates with 100 nm thick prepatterned ITO (6 pixels, 20 Ω/square) were cleaned using the following steps: (i) sonicated for 5 min in hot deionized (DI) water

Table 2. Spin-coated solar cells' performance. Average, standard deviation, and maximum values (in brackets) of the solar cell figures of merit measured on at least 11 pixels for each cell type.

		Number of pixels	PCE [%]	J_{SC} [mA cm^{-2}]	V_{OC} [V]	FF [%]
Cold	Forward	16	9.5 ± 0.3 (9.9)	15.4 ± 0.4 (16.1)	0.88 ± 0.01 (0.90)	70 ± 1 (72)
	Backward	16	9.6 ± 0.3 (10.2)	15.4 ± 0.4 (16.1)	0.89 ± 0.01 (0.91)	70 ± 2 (72)
Medium	Forward	12	11.2 ± 0.8 (12.2)	17.7 ± 0.3 (18.2)	0.90 ± 0.02 (0.93)	70 ± 3 (73)
	Backward	12	10.8 ± 0.7 (12.3)	17.5 ± 0.5 (18.2)	0.90 ± 0.01 (0.92)	69 ± 3 (73)
Hot	Forward	12	11.5 ± 0.8 (12.3)	18.2 ± 0.3 (18.6)	0.91 ± 0.03 (0.95)	69 ± 3 (72)
	Backward	11	11.9 ± 0.8 (12.8)	18.3 ± 0.3 (18.7)	0.92 ± 0.03 (0.95)	71 ± 2 (74)

www.MaterialsViews.com

ADVANCED
FUNCTIONAL
MATERIALS
www.afm-journal.de

FULL PAPER

(≈70 °C) with ≈1% Hellmanex III; (ii) rinsed twice in boiling DI water; (iii) sonicated for 5 min in isopropyl alcohol; (iv) rinsed in boiling DI water. Cleaned substrates were dried using compressed nitrogen and spin-coated with PEDOT:PSS. The steps followed for PEDOT:PSS and perovskite layer deposition in the preparation of the solar cells were identical to the steps detailed above for the preparation of the samples for SEM and nXRD, thus achieving identical layer thicknesses. The substrates coated with the perovskite layer were annealed for 90 min at 90 °C and transferred into a glovebox filled with nitrogen. [6,6]-Phenyl-C71-butyric acid methyl ester (PC$_{70}$BM, 99%) was dissolved in chlorobenzene (50 mg mL^{-1}) at ≈70 °C and stirred for 12 h (in the glovebox). The PC$_{70}$BM solution was then filtered using a 0.45 µm polytetrafluoroethylene (PTFE) filter and spin-coated (1000 rpm, 30 s) on the perovskite substrates to obtain a 120 nm thick layer. Devices were finally introduced in a thermal evaporator and coated (base pressure ≈1 × 10^{-6} mbar) with 5 nm Ca and 100 nm Al cathode through a metal mask. After the cathode was evaporated, the devices were encapsulated with a UV-curable epoxy and thin glass cover slips. JV scans were performed under a solar simulator (AM1.5, 100 mW cm^{-2}) with an aperture mask defining a device area of 0.025cm^2 and at a scan speed of 0.1 V s^{-1}.

Supporting Information

Supporting Information is available from the Wiley Online Library or from the author.

Acknowledgements

[1] A. Kojima, K. Teshima, Y. Shirai, T. Miyasaka, *J. Am. Chem. Soc.* **2009**, *131*, 6050.

[2] M. M. Lee, J. Teuscher, T. Miyasaka, T. N. Murakami, H. J. Snaith, *Science* **2012**, *338*, 643.

[3] H.-S. Kim, C.-R. Lee, J.-H. Im, K.-B. Lee, T. Moehl, A. Marchioro, S.-J. Moon, R. Humphry-Baker, J.-H. Yum, J. E. Moser, M. Grätzel, N.-G. Park, *Sci. Rep.* **2012**, *2*, DOI: 10.1038/srep00591.

[4] H. Zhou, Q. Chen, G. Li, S. Luo, T.-B. Song, H.-S. Duan, Z. Hong, J. You, Y. Liu, Y. Yang, *Science* **2014**, *345*, 542.

[5] Dyesol, EPFL Achieves 21% Efficiency for Perovskites, http://www.dyesol.com/media/wysiwyg/Documents/2015-asx-announcements/2015-12-08-DYE0397_-_EPFL_achieves_21_efficiency.pdf (accessed: April 2016).

[6] M. Liu, M. B. Johnston, H. J. Snaith, *Nature* **2013**, *501*, 395.

[7] J. M. Ball, M. M. Lee, A. Hey, H. J. Snaith, *Energy Environ. Sci.* **2013**, *6*, 1739.

[8] D. Liu, T. L. Kelly, *Nat. Photonics* **2014**, *8*, 133.

[9] N. J. Jeon, J. H. Noh, Y. C. Kim, W. S. Yang, S. Ryu, S. I. Seok, *Nat. Mater.* **2014**, *135*, 897.

[10] G. E. Eperon, V. M. Burlakov, P. Docampo, A. Goriely, H. J. Snaith, *Adv. Funct. Mater.* **2014**, *24*, 151.

[11] Q. Chen, H. Zhou, Z. Hong, S. Luo, H.-S. Duan, H.-H. Wang, Y. Liu, G. Li, Y. Yang, *J. Am. Chem. Soc.* **2013**, *136*, 622.

[12] A. Mei, X. Li, L. Liu, Z. Ku, T. Liu, Y. Rong, M. Xu, M. Hu, J. Chen, Y. Yang, *Science* **2014**, *345*, 295.

[13] M. A. Green, A. Ho-Baillie, H. J. Snaith, *Nat. Photonics* **2014**, *8*, 506.

[14] L. M. Pazos-Outón, M. Szumilo, R. Lamboll, J. M. Richter, M. Crespo-Quesada, M. Abdi-Jalebi, H. J. Beeson, M. Vručinić, M. Alsari, H. J. Snaith, B. Ehrler, R. H. Friend, F. Deschler, *Science* **2016**, *351*, 1430.

[15] D. B. Mitzi, in *Progress in Inorganic Chemistry* (Ed: K. D. Karlin), John Wiley & Sons, Inc., New York **1999**, Ch. 1.

[16] K. Liang, D. B. Mitzi, M. T. Prikas, *Chem. Mater.* **1998**, *10*, 403.

[17] G. E. Eperon, V. M. Burlakov, P. Docampo, A. Goriely, H. J. Snaith, *Adv. Funct. Mater.* **2014**, *24*, 151.

[18] A. T. Barrows, A. J. Pearson, C. K. Kwak, A. D. F. Dunbar, A. R. Buckley, D. G. Lidzey, *Energy Environ. Sci.* **2014**, *7*, 2944.

[19] Z. Wei, H. Chen, K. Yan, S. Yang, *Angew. Chem.* **2014**, *126*, 13455.

[20] K. Hwang, Y.-S. Jung, Y.-J. Heo, F. H. Scholes, S. E. Watkins, J. Subbiah, D. J. Jones, D.-Y. Kim, D. Vak, *Adv. Mater.* **2015**, *27*, 1241.

[21] P. Docampo, J. M. Ball, M. Darwich, G. E. Eperon, H. J. Snaith, *Nat. Commun.* **2013**, *4*, 2761.

[22] A. Dualeh, N. Tétreault, T. Moehl, P. Gao, M. K. Nazeeruddin, M. Grätzel, *Adv. Funct. Mater.* **2014**, *24*, 3250.

[23] Z. Xiao, Q. Dong, C. Bi, Y. Shao, Y. Yuan, J. Huang, *Adv. Mater.* **2014**, *26*, 6503.

[24] A. Sharenko, M. F. Toney, *J. Am. Chem. Soc.* **2016**, *138*, 463.

[25] W. Zhang, M. Saliba, D. T. Moore, S. K. Pathak, M. T. Hörantner, T. Stergiopoulos, S. D. Stranks, G. E. Eperon, J. A. Alexander-Webber, A. Abate, A. Sadhanala, S. Yao, Y. Chen, R. H. Friend, L. A. Estroff, U. Wiesner, H. J. Snaith, *Nat. Commun.* **2015**, *6*, DOI: 10.1038/ncomms7142.

[26] X. Tong, F. Lin, J. Wu, Z. M. Wang, *Adv. Sci.* **2016**, *3*, 1500201.

[27] D. T. Moore, H. Sai, K. W. Tan, D.-M. Smilgies, W. Zhang, H. J. Snaith, U. Wiesner, L. A. Estroff, *J. Am. Chem. Soc.* **2015**, *137*, 2350.

[28] W. J. Yin, T. Shi, Y. Yan, *Adv. Mater.* **2014**, *26*, 4653.

[29] E. Edri, S. Kirmayer, A. Henning, S. Mukhopadhyay, K. Gartsman, Y. Rosenwaks, G. Hodes, D. Cahen, *Nano Lett.* **2014**, *14*, 1000.

[30] J. S. Yun, A. Ho-Baillie, S. Huang, S. H. Woo, Y. Heo, J. Seidel, F. Huang, Y.-B. Cheng, M. A. Green, *J. Phys. Chem. Lett.* **2015**, *6*, 875.

[31] B. S. Tosun, H. W. Hillhouse, *J. Phys. Chem. Lett.* **2015**, *6*, 2503.

[32] D. W. de Quilettes, S. M. Vorpahl, S. D. Stranks, H. Nagaoka, G. E. Eperon, M. E. Ziffer, H. J. Snaith, D. S. Ginger, *Science* **2015**, *348*, 683.

[33] P.-W. Liang, C.-Y. Liao, C.-C. Chueh, F. Zuo, S. T. Williams, X.-K. Xin, J. Lin, A. K. Y. Jen, *Adv. Mater.* **2014**, *26*, 3748.

[34] C.-C. Chueh, C.-Y. Liao, F. Zuo, S. T. Williams, P.-W. Liang, A. K. Y. Jen, *J. Mater. Chem. A* **2015**, *3*, 9058.

[35] N. J. Jeon, J. H. Noh, Y. C. Kim, W. S. Yang, S. Ryu, S. I. Seok, *Nat. Mater.* **2014**, *13*, 897.

[36] S. Lilliu, J. Griffin, A. T. Barrows, M. Alsari, B. Curzadd, T. G. Dane, O. Bikondoa, J. E. Macdonald, D. G. Lidzey, *CrystEngComm* **2016**, *18*, 5448.

[37] M. Birkholz, *Thin Film Analysis by X-Ray Scattering*, Wiley-VCH, Weinheim, Germany **2006**.

[38] S. Pathak, A. Sepe, A. Sadhanala, F. Deschler, A. Haghighirad, N. Sakai, K. C. Goedel, S. D. Stranks, N. Noel, M. Price, S. Hüttner, N. A. Hawkins, R. H. Friend, U. Steiner, H. J. Snaith, *ACS Nano* **2015**, *9*, 2311.

[39] J. Schlipf, P. Docampo, C. J. Schaffer, V. Körstgens, L. Bießmann, F. Hanusch, N. Giesbrecht, S. Bernstorff, T. Bein, P. Müller-Buschbaum, *J. Phys. Chem. Lett.* **2015**, *6*, 1265.

[40] A. T. Barrows, S. Lilliu, A. J. Pearson, D. Babonneau, A. D. F. Dunbar, D. G. Lidzey, *Adv. Funct. Mater.* **2016**, *26*, 4934.

[41] R. Christian, *Rep. Prog. Phys.* **2000**, *63*, 233.

[42] G. E. Ice, J. D. Budai, J. W. L. Pang, *Science* **2011**, *334*, 1234.

[43] R. J. Davies, C. Koenig, M. Burghammer, C. Riekel, *Appl. Phys. Lett.* **2008**, *92*, 101903.

[44] M. Kastler, W. Pisula, F. Laquai, A. Kumar, R. J. Davies, S. Baluschev, M. C. Garcia–Gutiérrez, D. Wasserfallen, H. J. Butt, C. Riekel, G. Wegner, K. Müllen, *Adv. Mater.* **2006**, *18*, 2255.

[45] Z. Li, G. He, X. Wan, Y. Liu, J. Zhou, G. Long, Y. Zuo, M. Zhang, Y. Chen, *Adv. Energy Mater.* **2012**, *2*, 74.

[46] R. P. Kurta, L. Grodd, E. Mikayelyan, O. Y. Gorobtsov, I. A. Zaluzhnyy, I. Fratoddi, I. Venditti, M. V. Russo, M. Sprung, I. A. Vartanyants, S. Grigorian, *Phys. Chem. Chem. Phys.* **2015**, *17*, 7404.

[47] M. W. Bowler, M. Guijarro, S. Petitdemange, I. Baker, O. Svensson, M. Burghammer, C. Mueller-Dieckmann, E. J. Gordon, D. Flot, S. M. McSweeney, G. A. Leonard, *Acta Crystallogr., Sect. D* **2010**, *66*, 855.

[48] H. Lichtenegger, M. Muller, O. Paris, C. Riekel, P. Fratzl, *J. Appl. Crystallogr.* **1999**, *32*, 1127.

[49] B. Weinhausen, O. Saldanha, R. N. Wilke, C. Dammann, M. Priebe, M. Burghammer, M. Sprung, S. Köster, *Phys. Rev. Lett.* **2014**, *112*, 088102.

[50] N. Hrauda, J. Zhang, E. Wintersberger, T. Etzelstorfer, B. Mandl, J. Stangl, D. Carbone, V. Holý, V. Jovanović, C. Biasotto, L. K. Nanver, J. Moers, D. Grützmacher, G. Bauer, *Nano Lett.* **2011**, *11*, 2875.

[51] G. Capellini, G. Kozlowski, Y. Yamamoto, M. Lisker, C. Wenger, G. Niu, P. Zaumseil, B. Tillack, A. Ghrib, M. de Kersauson, M. El Kurdi, P. Boucaud, T. Schroeder, *J. Appl. Phys.* **2013**, *113*, 013513.

[52] A. Ricci, N. Poccia, G. Campi, B. Joseph, G. Arrighetti, L. Barba, M. Reynolds, M. Burghammer, H. Takeya, Y. Mizuguchi, Y. Takano, M. Colapietro, N. L. Saini, A. Bianconi, *Phys. Rev. B* **2011**, *84*, 060511.

[53] G. Campi, A. Ricci, N. Poccia, L. Barba, G. Arrighetti, M. Burghammer, A. S. Caporale, A. Bianconi, *Phys. Rev. B* **2013**, *87*, 014517.

[54] G. Campi, A. Bianconi, N. Poccia, G. Bianconi, L. Barba, G. Arrighetti, D. Innocenti, J. Karpinski, N. D. Zhigadlo, S. M. Kazakov, M. Burghammer, M. V. Zimmermann, M. Sprung, A. Ricci, *Nature* **2015**, *525*, 359.

[55] Y. Deng, E. Peng, Y. Shao, Z. Xiao, Q. Dong, J. Huang, *Energy Environ. Sci.* **2015**, *8*, 1544.

[56] T. Baikie, Y. Fang, J. M. Kadro, M. Schreyer, F. Wei, S. G. Mhaisalkar, M. Graetzel, T. J. White, *J. Mater. Chem. A* **2013**, *1*, 5628.

[57] K. Liang, D. B. Mitzi, M. T. Prikas, *Chem. Mater.* **1998**, *10*, 403.

[58] B.-W. Park, E. M. J. Johansson, B. Philippe, T. Gustafsson, K. Sveinbjörnsson, A. Hagfeldt, G. Boschloo, *Chem. Mater.* **2014**, *26*, 4466.

[59] B. Conings, L. Baeten, C. De Dobbelaere, J. D'Haen, J. Manca, H.-G. Boyen, *Adv. Mater.* **2014**, *26*, 2041.

[60] M. I. Saidaminov, A. L. Abdelhady, B. Murali, E. Alarousu, V. M. Burlakov, W. Peng, I. Dursun, L. Wang, Y. He, G. Maculan, A. Goriely, T. Wu, O. F. Mohammed, O. M. Bakr, *Nat. Commun.* **2015**, *6*, 1.

[61] A. Poglitsch, D. Weber, *J. Chem. Phys.* **1987**, *87*, 6373.

[62] C. C. Stoumpos, C. D. Malliakas, M. G. Kanatzidis, *Inorg. Chem.* **2013**, *52*, 9019.

[63] J.-H. Im, C.-R. Lee, J.-W. Lee, S.-W. Park, N.-G. Park, *Nanoscale* **2011**, *3*, 4088.

[64] E. Mosconi, A. Amat, M. K. Nazeeruddin, M. Graetzel, F. De Angelis, *J. Phys. Chem. C* **2013**, *117*, 13902.

[65] S. Colella, E. Mosconi, P. Fedeli, A. Listorti, F. Gazza, F. Orlandi, P. Ferro, T. Besagni, A. Rizzo, G. Calestani, G. Gigli, F. De Angelis, R. Mosca, *Chem. Mater.* **2013**, *25*, 4613.

[66] C. G. Schroer, G. Falkenberg, *J. Synchrotron Radiat.* **2014**, *21*, 996.

[67] G. Ashiotis, A. Deschildre, Z. Nawaz, J. P. Wright, D. Karkoulis, F. E. Picca, J. Kieffer, *J. Appl. Crystallogr.* **2015**, *48*, 510.